

A NEW METHOD FOR ANALYZING DEFECTS IN VENEER IMAGES: HYPOTHESIS TESTING BASED ON GAUSSIAN MIXTURE DECISION FUNCTION

Seyed V. SHOJAEDINI^{1*} Rasoul K. HAGHIGHI²

Abstract: *Accurate detection of defects plays a vital role in wood industry due to the direct relation between quality and price of wood products. To this aim, in this paper we introduce a new method in which we first use a hypothesis testing to distinguish between wood defects and clear wood. In the proposed scheme, firstly the natural pattern of veneer is removed by applying morphological enhancement, and in the second step the probable defects are estimated by a decision function based on Gaussian mixture concept. The performance of the proposed algorithm is evaluated on a data set of veneer images containing several types of surface defects. The results demonstrate that the proposed method extracts the defects approximately 8.2% better than its alternatives, in parallel with decreasing false detections by approximately 7.3%. The results obtained also show the considerable improvements in Accuracy and Precision of the proposed method compared to other examined methods, especially when a high detection rate (i.e. at least 90%) is desired.*

Key words: *defect detection, veneer images, hypothesis testing, natural pattern, Gaussian Mixture Model (GMM)*

1. Introduction

The effect of machining defects and environmental conditions such as temperature and rainfall cause different surface textures on wood products. Therefore, recognizing these surfaces is essential in order to evaluate them for further applications [14]. For several

decades, defect detection has been performed by experts.

Unfortunately this method is labor-intensive and inconsistent. Furthermore, its performance is degraded by human errors. In parallel with increasing wood products, automated inspection methods have been proposed in recent years [3], [13].

¹ Associate Professor in Electrical Engineering, Department of Electrical Engineering and Information Technology, Iranian Research Organization for Science and Technology, Iran.

² MSC in Electrical Engineering, Department of Electrical, Biomedical and Mechatronics Engineering, Qazvin Branch, Islamic Azad University, Qazvin, Iran.

Correspondence: Seyed V. Shojaedini; email: shojadini@irost.ir.

In automated approaches, firstly images are captured by using a camera from veneer specimens. In the next step, each captured image is segmented to flawless and defective regions. Finally, the characteristics of the defects are determined by classifying their morphologic features or other defect specifications [21]. Automatic defect detection is a vital step of the above procedure, because of its effect on classifying and recognizing defects [15]. Unfortunately, the performance of this step is hampered by some limitations such as poor contrast of defects, natural textures of wood surfaces which are so similar to many defects, the variety of textures of the wood surfaces, diversity and non-uniformity of colors of the wood surfaces, and noise. Several methods are proposed to solve the problems above [23].

A group of methods utilize thresholding to distinguish defects from other parts of the wood surface. Despite their easy implementation and low computational cost, these methods have problems such as different modes in the distribution of intensities and some small white spots or holes inside the defects [6], [17]. In other research abrupt changes in neighboring pixels is utilized to perform defect region. Unfortunately, these approaches often may not lead to meaningful connected region [2], [7]. Although region growing concept has been vastly utilized for defect detection, selecting primary pixels is one of the challenges of this approach [5]. Some other methods make use of texture features to distinguish the defects from the natural tissue of veneer. Although this idea may lead to extracting appropriate features in some special situations, it may be interpreted as the similarity between defects and the natural surface of the wood, which may be a major limitation for this approach [24]. Recently, model-based approaches have been developed for

segmenting veneer images. Although these approaches extract defects better than some existing methods, they suffer from limitations such as adjusting the control parameters of the model and falling in local minimums [12], [16].

In this paper, a novel method is introduced, which estimates defect regions by using a parametric mixture model. In the proposed method, firstly dependence of each pixel to defect or clear wood is demonstrated in a hypothesis test framework. To solve the hypothesis testing problem, a decision procedure is performed, which consists of: *i*) removing the natural tissue of veneer by applying morphological enhancement; *ii*) calculating a decision function based on a mixture of Gaussians; *iii*) estimating the parameters of Gaussian Mixture Model (GMM) by using the Expectation-Maximization method, and *iv*) performing Maximum Likelihood Estimation to assign each pixel of image to either defect or clear wood (i.e. each hypothesis) based on the estimated GMM. The paper is organized as follows. In Section 2, the proposed algorithm is introduced including hypothesis testing, image enhancement and estimating defect regions by using parametric model. In Section 3, the performance of the proposed method is evaluated by applying it on real captured images. In Section 4, the results obtained from the proposed method are compared with some alternative approaches to evaluate its effectiveness. The conclusion is presented in the last section of the paper.

2. Mathematical Model

Let I to be an image which has been captured from a veneer sample. This sample may contain some defects such as several types of knot (i.e. sound, edge, and crack), wane, and worm hole, as well as

natural tissue of wood. I_{mr} shows the pixel intensity which is located on row m and column r of the image I . Note that I_{mr} is in the range of $[0\ 255]$ and m, r are discrete numbers in the range between $[1\ 800]$ and $[1\ 247]$ respectively – i.e. the size of the images which are used in this article. Figure 1 shows the intensities belonging to a part of a sample image.

Now hypothesis testing is performed in such a way that the first hypothesis is defined as dependence of I_{mr} to the natural tissue of wood (i.e. g_{mr}) and noise (i.e. n_{mr}).

Both g_{mr} and n_{mr} are called the background of the image. The second hypothesis supposes that I_{mr} belongs to a defect on the wood surfaces (i.e. a_{mr}). The first hypothesis is named H_0 (i.e. null hypothesis) and the other one is named H_1 (i.e. alternate hypothesis) described in equation (1):

$$\begin{cases} H_0: I_{mr} = |g_{mr} + n_{mr}| \\ H_1: I_{mr} = |a_{mr} + g_{mr} + n_{mr}| \end{cases} \quad (1)$$

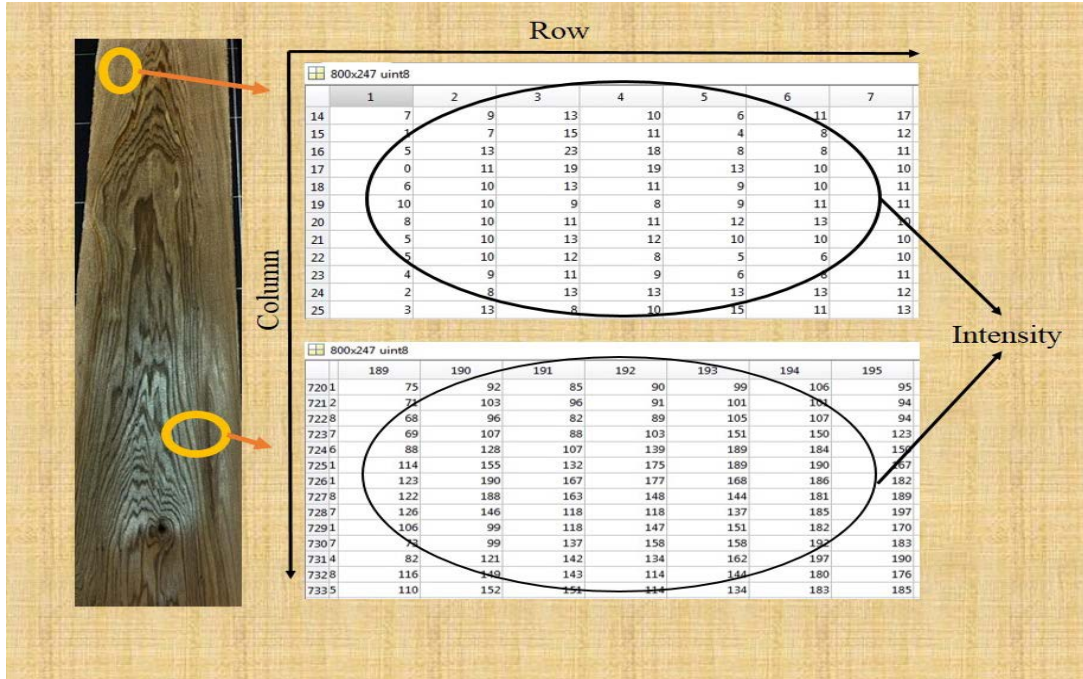


Fig. 1. Row and column of sample image

To estimate the location of probable defects, firstly the marker image I' is generated by rejecting the weak edges of the original image I as shown in equation (2). In equation (2), ξ is an arbitrary threshold which was selected equal to 0.85 by trial and error. Figure 2 shows the thresholding process by using the laplacian operator $\nabla^2(\cdot)$ on the original image I , in

which some region of the background of Figure 2 (a.) is omitted, which leads to Figure 2 (b.).

$$\begin{cases} I'_{mr} = I_{mr} & \max(\nabla^2 I_{mr}) > m \times r \times \xi \\ I'_{mr} = 0 & \text{otherwise} \end{cases} \quad (2)$$

In the next step, dilating is performed on the threshold image (such as Figure 2 (b)).

The dilating process is a morphological operation in which some points are selected as centers of several regions in an image and then all similar points around the region are gathered as described in equation (3) and shown in Figure 3. It is clear that the main effect of dilation is to the gradual enlargement of the boundaries of the foreground pixels. Thus, the areas of the foreground pixels grow in size while the holes within those regions become smaller. More details about this operation may be found in several image processing references such as [8], [20].

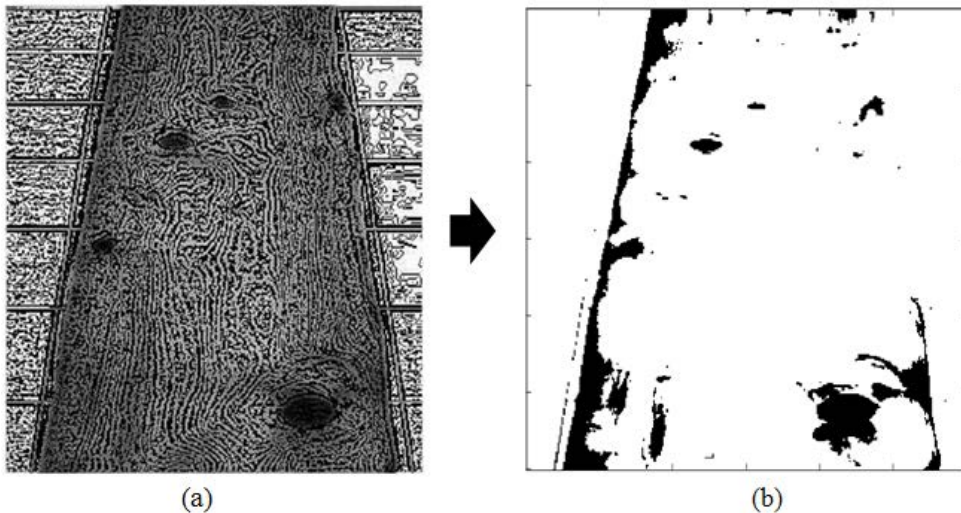


Fig. 2. a. – Laplacian of original image I_{mr} ; b. – Deleted weak edges of original image I_{mr}

The definition can be directly extended to gray level and RGB images. The dilation of an image I by structuring element B is denoted by $\delta_B(I)$ and is defined as the maximum of the translation of I by the vectors $-b$ of B . In other words, the dilated value of a given pixel is the maximum value of the image in the window defined by the structuring element when its origin is at x [20], as in the equation below:

The dilation of a set X by a structuring B is denoted by $\delta_B(X)$ and is defined as the locus of points x such that B hits X when its origin coincides with x .

$$\delta_B(X) = \{x \mid B_x \cap X \neq \Phi\} \quad (3)$$

The mentioned equation may be rewritten in terms of a union of set translations, the translations being defined as [20]:

$$\delta_B(X) = \bigcup_{b \in B} X_{-b} \quad (4)$$

$$[\delta_B(I)](x) = \max_{b \in B} I(x+b) \quad (5)$$

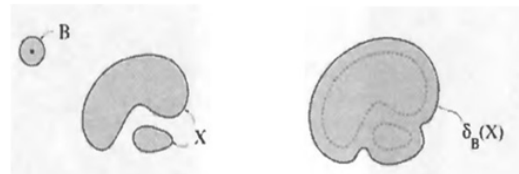


Fig. 3. Dilation δ of a set X by a disc B . The two connected components of X are connected by the dilation: B always hits X when it is placed in the channel separating

the particles [20]

Figure 4 shows the main steps of the dilating operation in which the intensities of those pixels which belong to clear wood have been highly attenuated. Then, the natural tissue of veneer becomes a homogeneous area by iterating the described dilation and the final symmetric image has been formed as Figure 4 (c.).

Ideally, subtracting Figure 4 (c.) from the original image in Figure 4 (a.) leads to an image which consists only of defect pixels,

but actually the resultant image may contain some pixels from other regions of the veneer surface as shown in Figure 4 (d.) [11].

Histograms are the basis for numerous spatial domain processing techniques. Histogram manipulation may be used effectively for image enhancement and may provide useful image statistics. It is also quite useful in other image processing applications, such as image compression and segmentation.

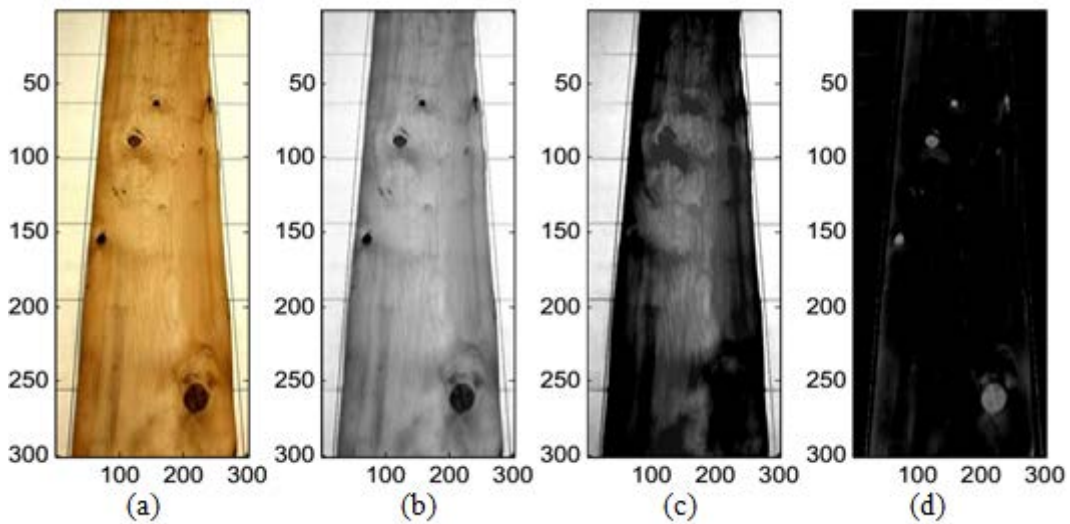


Fig. 4. Description of dilation on wood surface: a. – Original image; b. – attenuated; c. – homogeneous area of image; d. – subtracted image

The histogram of a digital image of wood surfaces with gray levels in the range $[0, L-1]$ is a discrete function $h(r_k) = n_k$, where r_k is the k_{th} gray levels and n_k is the number of pixels in the image having gray level r_k . The Sample of histograms of images in Figure 4 are shown in Figure 5 to illustrate the differences between the histograms of four images and to describe which of them has a better situation for use in the next process.

To distinguish the pixels belonging to defects from those pixels belonging to natural wood, the histogram of the image is

computed by using equation (6). The intensity of each pixel in the image is shown as z . Although q_p demonstrates abundance of the pixel in image. Also the Dirac function is equal to 1 when $z = p$, otherwise it is zero. Therefore, the histogram of each image may be constructed as [4], [9]:

$$W_r(z) = \sum_{p=0}^{255} q_p \delta(z - p) \quad (6)$$

The highest density values of the histogram are considered as centroids c_k of clusters CN_k as shown in Figure 6. Then, the minimum distance clustering is

$$\left\{ z \in CN_k \mid d_z^k = \min \|c_k - z\| \right\}, \quad k = 1, 2, \dots, K \quad (7)$$

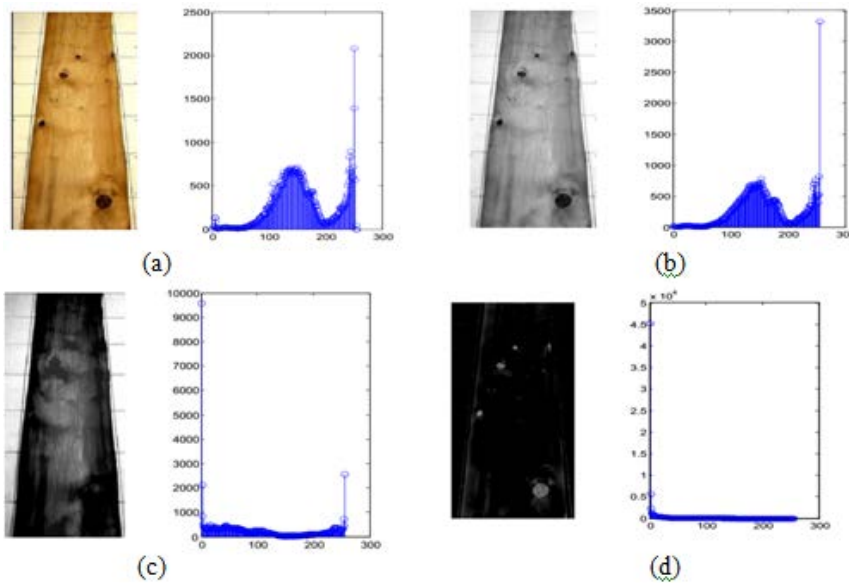


Fig. 5. Histograms of images in Figure 4: all images have been converted to gray level to obtain 2D histogram

In equation (7), each cluster is a sequence of pixels as $z_j^k = z_1^k, z_2^k, \dots, z_j^k, \dots, z_J^k$, the clusters are shown in Figure 7 by different colors, and each color has a centroid named c_k , in which z_j^k and J represent j 'th member and the number of pixels in each cluster. Furthermore, the distance may be calculated, for example d_1^2 , d_2^2 and so on.

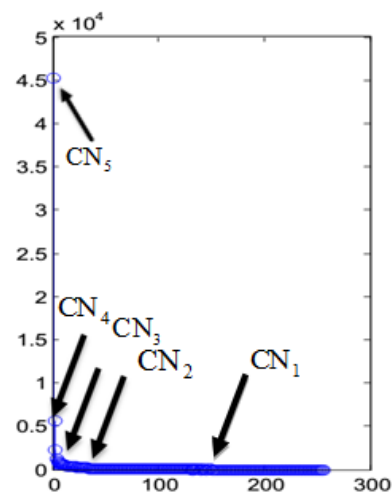


Fig. 6. Each centroid of clusters defined and the pixels of each cluster determined based on histogram value

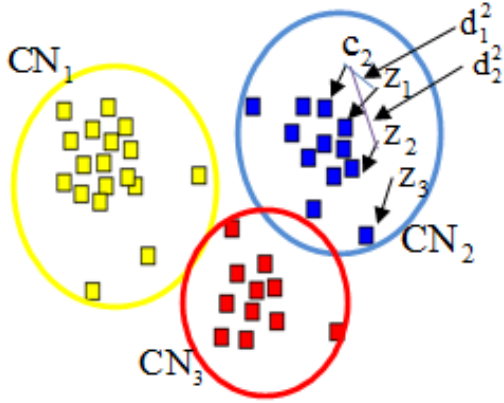


Fig. 7. Defined clusters and distance of pixel based on centroid

In the next step each cluster is modeled as a probability density function such as $f(z_j^k, \phi_k)$ where ϕ_k is its distribution parameters including mean μ_k , the variance σ_k^2 and the mixing parameter β_k and shaping parameter ω_k . The last parameter is defined as the peak of histogram and is estimated using equation (9). Figure 8 shows two probability distribution functions with different parameters which have determined ϕ_k for two clusters of Figure 6. This figure shows that every pixel in each cluster (i.e. z) may be determined by the variance σ_k^2 and the absolute mean value λ_k as in equation (10). Both of these parameters make an assessment between each pixel of clusters and the whole probability distribution. Therefore the dependence to each cluster may be measured by the probability model.

$$\phi_k = (\beta_k, \mu_k, \sigma_k^2, \omega_k) \quad (8)$$

$$\omega_k = L^{-1}(\alpha_k), \alpha_k = \frac{\lambda[|z|]}{\sigma_k^2} \quad (9)$$

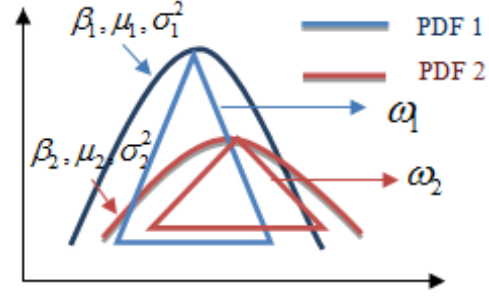


Fig. 8. Probability density function with different parameters

In the equation above $\lambda_k[|z|]$ is called the absolute mean value and is calculated as in equation (10). The absolute mean value examines the dependency between the probability distribution and the cluster.

$$\lambda_k[|z|] = \frac{1}{M \times R} \sum_{j=1}^J \sum_{k=1}^K |z_j^k - \mu_k| \quad (10)$$

A simple Gaussian distribution is shown in equation (11). This distribution has variance and mean values to generate different shapes as in Figure 9, which is not suitable to detect the boundary of clusters, while the shaping parameter ω_k makes use of $L(\alpha_k)$. Furthermore $L(\cdot)$ is Generalized Gaussian ratio function [19].

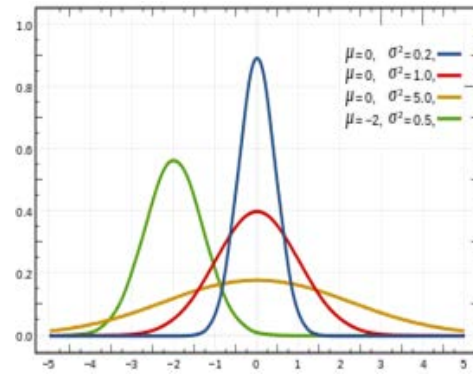


Fig. 9. Simple Gaussian distribution

$$f(p) = a e^{-\frac{(p-b)^2}{2c^2}} \quad (11) \quad \Gamma(\alpha_k) = \int_0^{+\infty} t^{\alpha_k-1} e^{-t} dt, \alpha_k > 0 \quad (13)$$

$$L(\alpha_k) = \frac{\Gamma\left(\frac{2}{\alpha_k}\right)}{\Gamma\left(\frac{1}{\alpha_k}\right)\Gamma\left(\frac{3}{\alpha_k}\right)} \quad (12)$$

In the equations above Γ represents the Gamma function and is defined as:

$$f(z_j^k, \phi_k) = \frac{1}{2\Gamma\left(1 + \frac{1}{\omega_k}\right) A(\omega_k, \sigma_k)} \times \exp\left[-\left|\frac{(z_j^k - \mu_k)}{A(\omega_k, \sigma_k)}\right|^{\omega_k}\right] \quad (14)$$

Based on equation (11) we have:

$$a = \frac{1}{2\Gamma\left(1 + \frac{1}{\omega_k}\right) A(\omega_k, \sigma_k)} e^{-\frac{(p-b)^2}{2c^2}} = e^{\left[-\left|\frac{(z_j^k - \mu_k)}{A(\omega_k, \sigma_k)}\right|^{\omega_k}\right]} \quad (15)$$

in which the scaling factor for the Gaussian model is defined as:

$$A(\omega_k, \sigma_k) = \left[\frac{\sigma_k^2 \Gamma\left(\frac{1}{\omega_k}\right)}{\Gamma\left(\frac{3}{\omega_k}\right)}\right]^{\frac{1}{2}} \quad (16)$$

The mixture of all PDFs (i.e. clusters) may perform an aggregated distribution as:

$$f(z, \phi) = \sum_{k=1}^K \beta_k f(z_j^k, \phi_k) \quad (17)$$

The PDF of each cluster is considered as a Gaussian Distribution Model (GDM) as shown in Figure 9 and in equation (11). This concept is used to distinguish clear regions from defect areas by shaping and mixing parameters based on the PDF model for pixels.

To estimate the most optimum parameters for PDFs (i.e. the best clusters), the Expectation Maximization (EM) Algorithm is utilized in this article. EM algorithm tries to detect defect regions with minimum error ratio. Each iteration (i.e. v) of the EM algorithm consists of two steps. The E-step that computes the expected complete data Log Likelihood function $\psi(\phi, \phi_k^{(v)})$ is demonstrated in Figure 10.

$$\psi(\phi, \phi_k^{(v)}) = \sum_{j=1}^J \sum_{k=1}^K [\log(\beta_k^{(v)} f(z_j^k, \phi_k^{(v)}))] \times u_k(z_j^k, \phi_k^{(v)}) \quad (18)$$

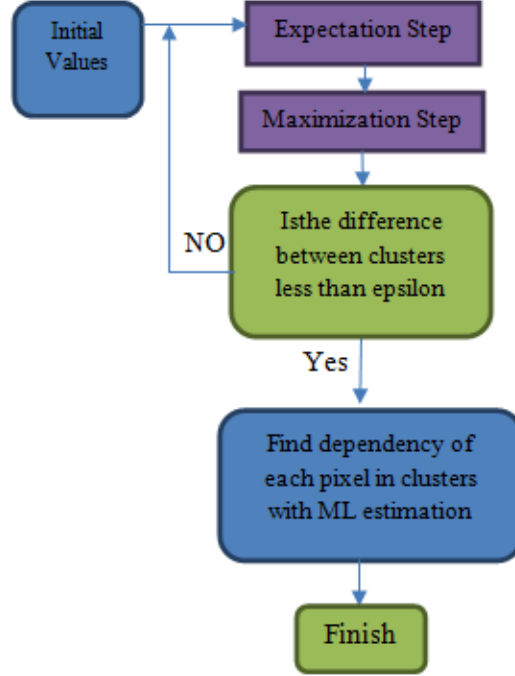


Fig. 10. Diagram of the Gaussian Mixture Decision Function

Figure 11 shows an illustrative example from cluster number (1), in which $\psi(\phi, \phi_1^1)$ at first has a primary value that may be updated in successive iterations to $\psi(\phi, \phi_1^2)$ and $\psi(\phi, \phi_1^3)$ with new values which have been computed from equations (21), (22), and (23).

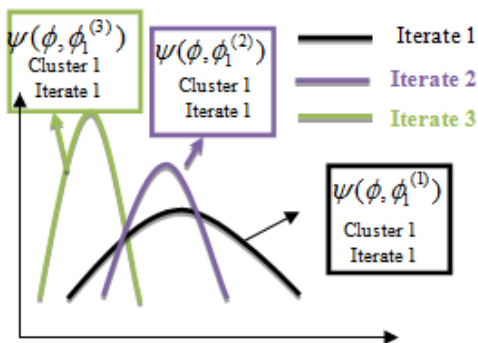


Fig. 11. Probability density function with different parameters

In equation (18), $u_k(z_j^k, \phi_k^{(v)})$ shows a Posterior Probability and is computed as below:

$$u_k(z_j^k, \phi_k^{(v)}) = \frac{\beta_k^{(v)} f(z_j^k, \phi_k^{(v)})}{\sum_{k=1}^K \beta_k^{(v)} f(z_j^k, \phi_k^{(v)})} \quad (19)$$

In the M-step $\phi_k^{(v+1)}$ (i.e. the new estimation of parameters) is calculated by using equations (20), (21), and (22) to calculate Log Likelihood function $\psi(\phi, \phi_k^{(v)})$.

$$\beta_k^{(v+1)} = \frac{1}{J} \sum_{j=1}^J u_k(z_j^k, \phi_k^{(v)}) \quad (20)$$

$$\mu_k^{(v+1)} = \frac{\sum_{j=1}^J u_k(z_j^k, \phi_k^{(v)}) z_j^k}{\sum_{j=1}^J u_k(z_j^k, \phi_k^{(v)})} \quad (21)$$

$$\sigma_k^{(v+1)} = \left[\frac{\sum_{j=1}^J u_k(z_j^k, \phi_k^{(v)}) \left(\frac{\Gamma(\frac{3}{\omega})}{\omega \Gamma(\frac{1}{\omega})} \right) |z_j^k - \mu_k^{(v)}|^{\frac{1}{\omega_k}}}{\sum_{j=1}^J u_k(z_j^k, \phi_k^{(v)})} \right]^{\frac{1}{\omega_k}} \quad (22)$$

Process stops when the difference between ϕ^{v+1} and ϕ^v is less than ε . That

$$\begin{cases} H_0: \max_k f(\text{Im } r, \phi_k) > \chi \Rightarrow I_{mr} = |g_{mr} + n_{mr}| \\ H_1: \max_k f(\text{Im } r, \phi_k) < \chi \Rightarrow I_{mr} = |a_{mr} + g_{mr} + n_{mr}| \end{cases} \quad (23)$$

The complete defect detection procedure is described as a pseudo code in Figure 12.

```

Procedure of Proposed Algorithm
□ Omitting natural tissues of wood surfaces
To make marker.
Dilating original image by using marker.
Obtaining background area from consecutive dilations.
Assigning seed class regions for defects.
□ Deciding based of parametric mixture model.
Performing histogram of the image with omitted background.
Construction of Clusters by using minimum distance clustering
concept.
Estimating distribution parameters of each cluster ( $\phi_k$ ) by using
EM approach.
Mixing clusters to perform the best aggregate PDF.
■ Iteration Process
For each iteration
✓ E-step
Compute the expected complete data Log Likelihood function
( $\psi(\phi, \phi_k^v)$ )
✓ M-Step
Finds the  $(v+1)^{th}$  estimation ( $\phi^{(v+1)}$ ) by updating
( $\beta_k^{(v+1)}$ ), ( $\mu_k^{(v+1)}$ ) and ( $\sigma_k^{(v+1)}$ )
If  $|\phi^{v+1} - \phi^v| > \varepsilon$ 
then  $\phi^{v+1} = \phi^v$ 
return E-step
Else
continue
End if
End Iteration
Assigning each pixel into proper cluster (i.e. defect or background)
Complete segmentation

```

Fig.12. Pseudo code of the proposed algorithm

3. Tests and Results

The proposed algorithm was applied on real data. The data set were represented by

several veneer images containing various types of natural textures and defects. Table 1 depicts some important parameters corresponding to images and defects.

Table 1

Specifications of examined veneer images and defects

Specification of Images	Value	Specification of Defects	Value
Number of images	50 frames	Wood types	Soft, Hard
Average contrast	25%	Min and Max length of defect	18,54 (pixel)
Frame size	410,510 pixels	Min and Max width of defect	10,28 (pixel)

The proposed method was implemented using Mat lab 2014. Additionally, Co-occurrence Matrix Thresholding (CMT) [10] and K-Means Clustering (KMC) [1] methods were implemented for comparison with the proposed algorithm. The captured images were first processed using manual detection to exact defects as ground truth, then the performance of each algorithm was determined by comparing its results with the ground truth.

Figures 15 (b.) to 15 (d.) show the results obtained from applying the proposed method and its alternatives on a sample image which is shown in Figure 15 (a.). Figure 15 (b.) shows that the proposed method has extracted all 5 defects on the veneer surface. Moreover, Figure 15 (c.) shows that CMT method has missed no defect, but has extracted 3 false objects. Figure 15 (d.) shows the result obtained from KMC which has missed 3 defects and has extracted 5 false defects instead. In similar manner, Figures 16 (b.) to 16 (d.) show the results obtained from applying all methods on another sample image which is shown in Figure 16 (a.). Figure 16 (b.) shows that the proposed algorithm has extracted the defect without detecting any false. As shown in Figure 16 (c.) CMT method has extracted the same defect but with a false detection. Figure 16 (d.) shows

that KMC algorithm has detected the defect but in parallel with 4 false objects. The existence of some bright background objects which may be detected as defects is one of the challenges in the veneer defect detection problem. Therefore, in another scenario the images with no defects captured from veneer were examined. An example of this scenario is shown in Figure 17 (a.). Figures 17 (b.) to Figure 17 (d.) show the results of applying the method mentioned on the veneer sample which is shown in Figure 17 (a.). Figure 17 (b.) shows that although the proposed algorithm has not extracted any defect, its alternatives have led to several false detections.

4. Performance Evaluation

Real data were analyzed using CMT, KMC, and the proposed method, and the results were compared with manual detection by using five standard parameters [10], [22], and [24] which have been defined as equations (24) to (28). These definitions have been selected to illustrate different specifications in wood surfaces. For this purpose, in Figures 13 and 14 the concept of each equation in (24) to (28) is illustrated visually.

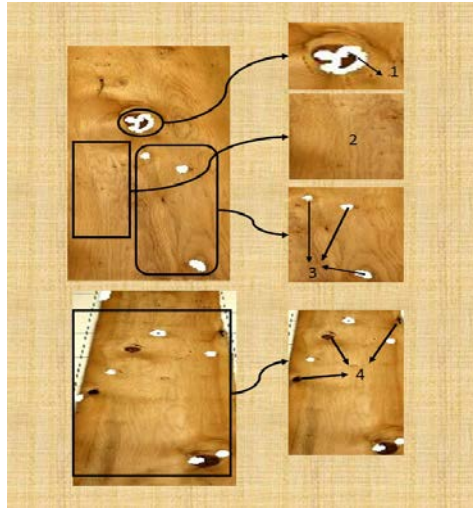


Fig. 13. *Descriptions of equations (24) to (27)*

In these equations, true positive (TP) is defined as the number of correctly identified defects as shown in Figure 13 – number 1. The natural pattern of the wood which has been properly undetected is known as true negative (TN), as shown in Figure 13 – number 2. False positive (FP) is defined as the number of other defects that is incorrectly identified, as shown in Figure 13 – number 3. False negative (FN) is when a test result indicates that the condition failed and the method may not define the defect as shown in Figure 13 –

number 4. The first comparison parameter was true positive rate (TPR) and is defined as:

$$\text{TPR} = \frac{\text{TP}}{\text{TP} + \text{FN}} \quad (24)$$

The second evaluation parameter was false positive rate (FPR) which is defined as:

$$\text{FPR} = \frac{\text{FP}}{\text{FP} + \text{TN}} \quad (25)$$

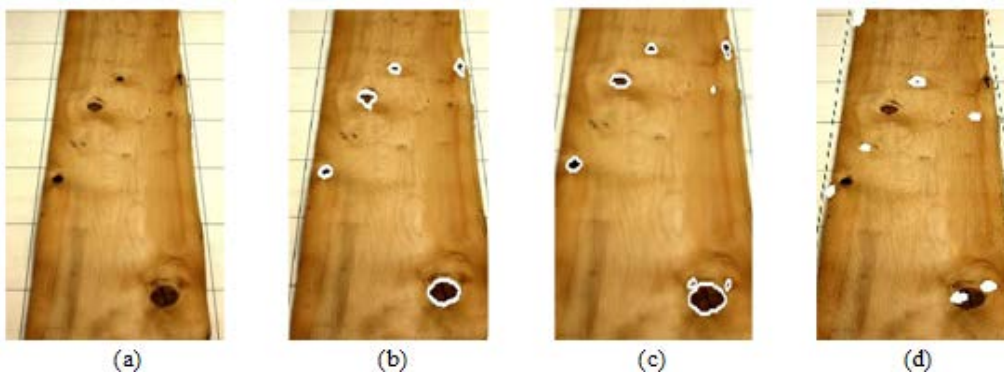


Fig. 15. *The results obtained from examined algorithms on a captured image containing clear tissue of veneer and defects: a).The original image and its detection results by using (b).proposed, (c).CMT and (d).KMC algorithms*

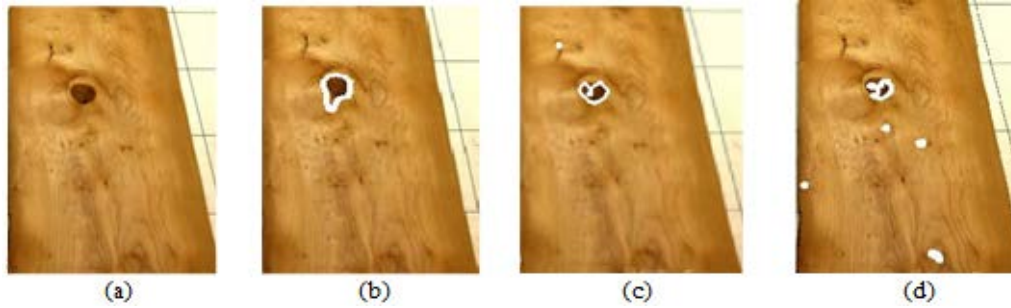


Fig. 16. The results obtained from the examined algorithms on a captured image containing clear tissue of veneer and defects: (a). the original image and defects detection results with different algorithms (b).proposed, (c). CMT and (d).KMC

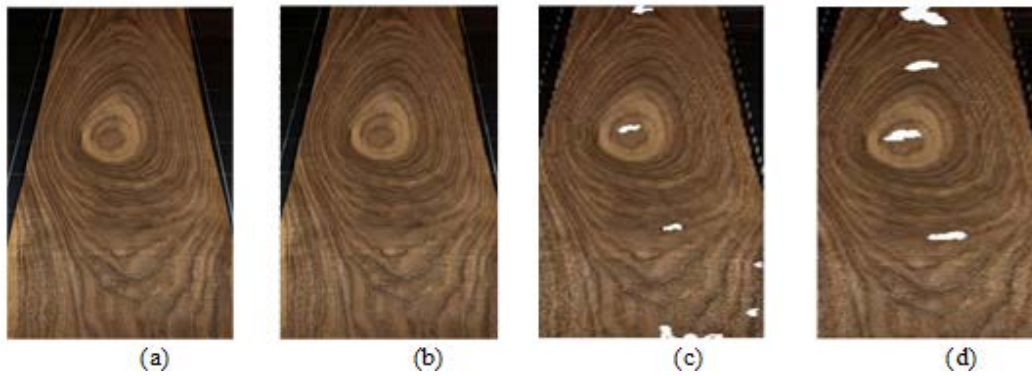


Fig. 17. The results obtained from examined algorithms on a captured image containing clear tissue of veneer: (a).the original image and defects detection results by using (b).proposed, (c). CMT and (d).KMC algorithms

The third evaluation parameter was precision (P) which is defined as:

$$P = \frac{TP}{TP + TN} \quad (26)$$

Another parameter was Accuracy (A) which is defined as:

$$A = \frac{TP + TN}{TP + FP + TN + FN} \quad (27)$$

The last evaluation parameter was defect accuracy (DA), which is the ratio of the number of detected true defect pixels to the total number of defect pixels as shown in Figure 14 and in the following equation:

$$DA = \frac{NDTP}{TNDP} \quad (28)$$

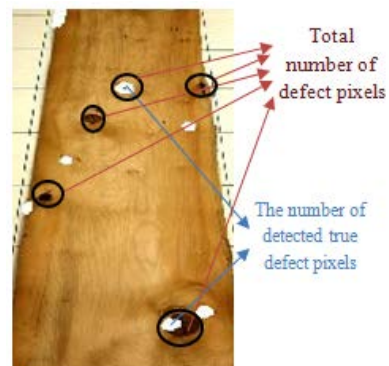


Fig. 14. Descriptions of Defect Accuracy (DA) in equation (29)

Changes of detection rate versus false detection rate (e.g. ROC curve) have been obtained for all the methods examined as shown in Figure 18.

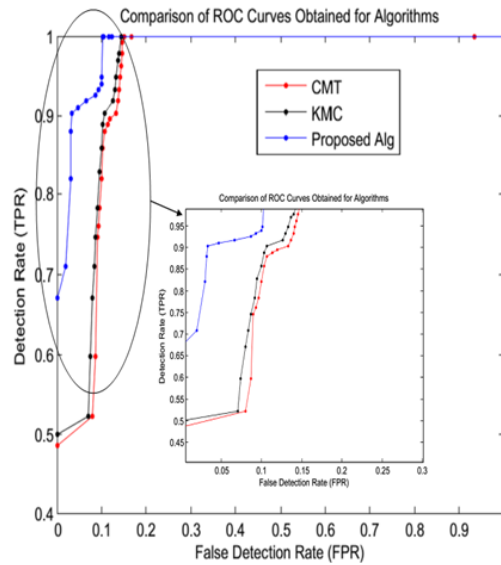


Fig. 18. ROC curves obtained for the CMT (red line), KMC (black line) and the proposed algorithm (blue line)

For a better interpretation of the results, the values FPR=10% and TPR=90% were considered as typical acceptable thresholds for false and true detection rates, which led to Tables 2 and 3. By exploiting the tables obtained, a better performance of the proposed algorithm was proven compared to other algorithms in such a way that the

proposed algorithm achieved TPR, 12% and 8.2% better than CMT and KMC, respectively. Moreover, the precision of the proposed algorithm was 1.6% and 2.2% higher than CMT and KMC algorithms.

Table 2

The parameters obtained for examined algorithms in FPR=10%

Algorithms	TPR	P	A	DA
CMT	82%	44%	90%	60%
KMC	85.8%	43.4%	91.2%	42%
Proposed Algorithm	94%	45.6%	91.5%	87%

Table 3

The parameters obtained for examined algorithms in TPR=90%

Algorithms	FPR	P	A	DA
CMT	13.3%	37.7%	87.7%	64%
KMC	10.6%	43%	90%	46.9%
Proposed Algorithm	3.3%	70%	96.2%	85%

Defect Accuracy of the proposed algorithm shows 27% and 45% improvement against its alternatives, all in presence of a typically low FPR=10%. Another performance evaluation was performed in typically high TPR equal to 90%. In this case the proposed algorithm surpassed FPR by 10% and was 7.3% better than CMT and KMC. Furthermore, the precision of the proposed algorithm was 32.3% and 27% higher than its alternatives. These improvements were 8.5% and 6.2% for the accuracy parameter. Finally, the defect accuracy for the proposed method was 21% and 38.1% better than of the other methods.

5. Conclusions and Remarks

This paper introduced a new method for automated defect detection in images captured from veneer samples. The proposed algorithm consisted in removing the natural tissue of the veneer by using morphologic operators, constructing a parametric model to express the regions of the veneer and finally Maximum Likelihood Estimation to determine where each pixel belongs: into defect or clear wood.

To evaluate the effectiveness of the proposed algorithm, its performance was compared to some existing methods in terms of five standard parameters. It was observed that the proposed algorithm has extracted defects at least 8.2% better than other methods and the precision, accuracy and defect accuracy were at least 1.6%, 0.3%, and 27% higher and better than the other methods in the presence of typically low FPR equal to 10%. Furthermore, it has been shown that FPR of the proposed algorithm has been at least 7.3% better than of the other methods. This superiority was at least 27%, 6.2% ,and 21% in terms of precision, accuracy and defect accuracy, all in TPR=90%. Consequently, it may be concluded that the proposed method may be

used as a suitable alternative for the detection of defects in images of veneer samples.

References

1. Alapuranen P., Westman T., 1992. Automatic visual inspection of wood surfaces. In: Proceedings 11th IAPR International Conference on, Conference A: Computer Vision and Applications, vol. 1, pp. 371-374.
2. Belknap R., 1999. Softwarevision: understanding other edge- and line-based segmentation techniques. In: Vision Systems Design, vol. 4(4), pp. 25-28.
3. Bond B.H., 1998. Characterization of wood features using color, shape and density parameters. Doctoral Thesis. Department of Wood Science and Forest Products, Virginia Polytechnic Institute and State University, Blacksburg.
4. Chan T., Shen J.J., 2005. Image processing and analysis: variational. PDE, Wavelet, and Stochastic Methods. Handbook. Society for Industrial and Applied Mathematics Philadelphia.
5. Chen L., Wang K., Xie Y. et al., 2014. The segmentation of timber defects based on color and the mathematical morphology. In: Optik – International Journal for Light and Electron Optics, vol. 125(3), pp. 965-967.
6. Funck J.W., Zhong Y., Butler D.A. et al., 2003. Image segmentation algorithms applied to wood defect detection. In: Computers and Electronics in Agriculture, vol. 41, pp. 157-179.
7. Gasim Harjoko A., Hartati S., 2013. Merging feature method on RGB image and edge. In: International Journal of Computer Science and Information Technologies, Detection Image for Wood Identification, vol. 4(1), pp. 188-193.

8. Ghosh P.K., Deguchi K., 2008. Mathematics of shape description: A morphological approach to image processing and computer graphics. Handbook John Wiley & Sons (Asia) Pte Ltd, Singapore.
9. Gonzalez R.C., Woods R.E., 2002. Digital image processing. Handbook. Second Edition. Prentice Hall, Upper Saddle River, New Jersey.
10. Hu C., Min X., Yun H. et al., 2011. Automatic detection of sound knots and loose knots on sugi using gray level co-occurrence matrix parameters. In: *Annals of Forest Science*, vol. 68, pp. 1077-1083.
11. Irving B.J., Taylor P., Todd-Pokropek A., 2009. 3D segmentation of the airway tree using a morphology based method. Second International Workshop on Pulmonary Image Analysis, MICCAI.
12. Kass M., Witkin A., Terzopoulos. D., 1988. Snakes: active contour models. In: *International Journal of Computer Vision*, vol. 1(4), pp. 321-331.
13. Kauppinen H., 1999. Development of a color machine vision method for wood surface inspection. Academic Dissertation. Department of Electrical Engineering and Infotech Oulu, University of Oulu, Finland.
14. Lemaster R.L., 2004. Development of an optical profilometer and the related advanced signal processing methods for monitoring surface quality of wood machining applications. Doctoral Thesis. Department of Wood and Paper Science, North Carolina State University.
15. Lu D., Weng Q., 2007. A survey of image classification methods and techniques for improving classification performance. In: *International Journal of Remote Sensing*, vol. 28(5), pp. 823-870.
16. Mu H., Qi D., Zhang M. et al., 2008. Image edge detection of wood defects based on Multi-fractal analysis. In: *IEEE International Conference on Automation and Logistics (ICAL)*, pp. 1-3.
17. Sahoo P.K., Soltani S., Wong A.K.C., 1988. A survey of thresholding techniques. In: *Computer Vision, Graphics and Image Processing*, vol. 41(2), pp. 233-260.
18. Sateesh Kumar H.C., Raja K.B, Venugopal K.R. et al., 2009. Automatic image segmentation using wavelets. In: *International Journal of Computer Science and Network Security (IJCSNS)*, vol. 9(2), pp. 305-313.
19. Sharifi K., Garcia A.L., 1995. Estimation of shape parameter for generalized gaussian distribution in subband decomposition of video. In: *IEEE Transactions on Circuits and Systems for Video Technology*, vol. 5(1), pp. 52-56.
20. Soille P., 2004. Morphological image analysis: Principle and Applications. Second Edition. Springer-Verlag, Germany.
21. Srikanteswara S., 1997. Feature identification in wooden boards using color image segmentation. Master of Science Dissertation. Virginia Polytechnic Institute and State University.
22. Todoroki C.L., Lowell E.C., Dykstra D., 2010. Automated knot detection with visual post-processing of Douglas-fir veneer images. In: *Computers and Electronics in Agriculture*, vol. 70, pp. 163-171.
23. Unsalan C., Ercil A., 1998. Defect inspection of wood surfaces. Report (FBE-IE-08/97-12), Bogazici University, Bebek, Istanbul, Turkey.
24. Zhong Y., 1995. Image segmentation for defect detection on veneer surfaces. Doctoral Thesis. Includes Bibliographical References, Oregon State University, Leaves.